Structure tensor based analysis of cells and nuclei organization in tissues

Wenxing Zhang, Jérôme Fehrenbach, Annaick Desmaison, Valérie Lobjois, Bernard Ducommun, Pierre Weiss

Structure tensor based analysis of cells and nuclei organization in tissues

Wenxing Zhang[1,2,3], Jérôme Fehrenbach[1,2,4,5], Annaïck Desmaison[1,2], Valérie Lobjois[1,2], Bernard Ducommun[1,2,6], and Pierre Weiss [*1,2,4,5]

[1]CNRS, ITAV-USR3505, Toulouse, France.
[2]Université de Toulouse, ITAV-USR3505, Toulouse, France.
[3]School of Mathematical Sciences, University of Electronic Science and Technology of China, Chengdu, China.
[4]CNRS, IMT-UMR5219, Toulouse, France.
[5]Université de Toulouse, IMT-UMR5219, Toulouse, France.
[6]CHU de Toulouse, Toulouse, France.

July 23, 2014

Abstract

Motivation: Extracting geometrical information from large 2D or 3D biomedical images is important to better understand fundamental phenomena such as morphogenesis. We address the problem of automatically analyzing spatial organization of cells or nuclei in 2D or 3D images of tissues. This problem is challenging due to the usually low quality of microscopy images as well as their typically large sizes.

Results: The structure tensor is a simple and robust descriptor that was developed to analyze textures orientation. Contrarily to segmentation methods which rely on an object based modelling of images, the structure tensor views the sample at a macroscopic scale, like a continuum. We propose an original theoretical analysis of this tool and show that it allows quantifying two important features of nuclei in tissues: their privileged orientation as well as the ratio between the length of their main axes. A quantitative evaluation of the method is provided for synthetic and real 2D and 3D images. As an application, we analyze the nuclei orientation and anisotropy on multicellular tumor spheroids cryosections. This analysis reveals that cells are elongated in a privileged direction that is parallel to the boundary of the spheroid.

Availability: Source codes are available at `http://www.math.univ-toulouse.fr/~weiss/`

[*]Corresponding author: pierre.armand.weiss@gmail.com

1 Introduction

The advent of new imaging technologies allows observing biological samples with an unprecedented spatial, temporal and spectral resolution. It offers new opportunities to perform systematic studies of geometrical configurations of cells or nuclei in their micro-environment to better understand the fundamental processes involved in morphogenesis or tumor growth [22, 18].

Due to the huge amount of data contained in large images, automatic procedures are however essential to assess cells properties such as location, size, orientation, aspect ratio, etc... The lack of robust, fast and universal procedures to provide such a geometric description is probably one of the main obstacles to exploit the full potential of images.

The mainstream approach to analyze image contents nowadays consists in *segmenting* each cell/nuclei independently [22, 24]. A precise segmentation completely describes the geometrical contents of images and is often regarded as the best source of information one can hope for. However biological images often suffer from many degradations. For instance, in fluorescence microscopy, light scattering, absorption or poor signal to noise ratio strongly impair image quality, especially in 3D. In many situations it is therefore hopeless to perform a proper image segmentation. Moreover, in cases where large cell populations are investigated, a complete segmentation (i.e. a precise description of the objects boundaries) still brings more information than needed to understand the overall geometrical distribution.

In this paper we therefore pursue a somehow less ambitious goal. We adopt a macroscopic point of view and consider the biological sample as a continuous medium. This idea stems from mathematical models that describe tissues as continuous media such as incompressible fluids, elastic or viscoelastic materials [6, 1, 17, 16, 4]. Our main contribution is to show through both theoretical and numerical results that the so-called *structure tensor* [12, 3, 13], provides a fast, robust and precise enough tool to retrieve cells orientation and anisotropy in 2D and in 3D. We show the following original results:

- While the structure tensor is usually implemented to assess texture orientations, we show that it also allows quantifying precisely the anisotropy of cells or nuclei. This is done by analyzing the method behavior on fields of functions with ellipsoidal isosurfaces.

- The proposed mathematical analysis also allows quantifying the method bias. It shows that a very good estimation can be expected even when very few nuclei are locally similar (in the sense that they can be well approximated by the same ellipsoid).

- We show that the method is invariant under contrast changes.

We also perform various experiments to validate our theoretical findings. We assess the structure tensor efficiency on synthetic and real 2D and 3D images. Its output is compared to ground-truth obtained analytically in case of synthetic data or manually in case of real data. These comparisons show that the structure tensor allows to quickly assess cells organization at a large scale. We finish the paper by providing an example of application to the analysis of geometrical configurations of nuclei in multicellular tumor spheroids.

Related work The structure tensor has already been used in various contexts of biological imaging. One of its main applications is coherence enhancing or diffusion [33, 34, 24] which usually allows improving images quality without degrading their geometrical content too much. It was also used to analyze geometrical features such as fibers orientations in 2D and 3D [23, 20, 10, 26, 11]. The works [26, 11] also come with an ImageJ plugin `http://bigwww.epfl.ch/demo/orientation/`. This plugin has a nice interface and can be used to reproduce some experiments of our paper. The authors of these two references mention that the structure tensor allows quantifying the orientation and the isotropy properties of a region of interest. However, the isotropy is defined in a way different from the present paper and the authors do not state precisely how this information relates to the image contents.

Paper organization The rest of the paper is organized as follows. Notation is introduced in Section 2. Section 3 constitutes the theoretical part of the paper. We introduce the structure tensor and demonstrate its properties when applied to images that consist in fields of functions with ellipsoidal isosurfaces. In Section 4, we illustrate the method on synthetic and real 2D and 3D data.

2 Notation

For any $x, y \in \mathbb{R}^d$, the angle in degrees between x and y is denoted $\angle(x, y)$, this angle lies in $[0°, 90°]$. The ℓ_p-norm of $x \in \mathbb{R}^d$ is denoted $\|x\|_p$ and defined by $\|x\|_p := (\sum_{i=1}^d |x_i|^p)^{1/p}$. The positive semidefiniteness of a matrix A is denoted $A \succeq 0$. The spectral norm of a matrix A is denoted $\|A\|_2$. We denote $\bar{A} := A/\|A\|_2$ the normalized version of A. The largest (resp. smallest) eigenvalue of A is denoted $\lambda_{\max}(A)$ (resp. $\lambda_{\min}(A)$). The notation Id denotes the identity operator. Given a vector $x \in \mathbb{R}^d$, we let $\mathrm{diag}(x)$ denote a diagonal matrix whose diagonal elements are the entries of x. The Givens transform, denoted by $R_{ij}^\theta \in \mathbb{R}^{d\times d}$, represents a counter-clockwise rotation for an angle θ in the (i, j)-coordinates plane. In the particular case $d = 2$, it is abbreviated R^θ.

3 Theoretical analysis

The structure tensor appeared in the field of image processing in the late 80's [12] for the problem of interest point detection. It was then justified theoretically and popularized in different contexts such as interest point detection [12, 15], texture analysis [3, 13], representation of flow-like images [25], optical flow problems [19] and anisotropic or coherence enhancing diffusion [24, 33, 34].

In this section, we first recall the definition of structure tensor, then show its capability of analyzing fields of locally coherent ellipses (in 2D) or ellipsoids (in 3D). The motivation for introducing fields of ellipses is that images such as Figure 3 are a rather good approximation of certain dense tissues such as microtumors. To the best of our knowledge, even though fields of locally coherent ellipsoids share some similarities with flow-like images, the proposed theoretical analysis and results are original and shed a novel light on the structure tensor.

3.1 Preliminary facts about the structure tensor

Let $u : \mathbb{R}^d \to \mathbb{R}$ denote a grayscale image. In this paper, we restrict on the practical cases $d = 2$ and $d = 3$, although the theory is valid in any dimension. For ease of exposition, we assume that $u \in C^1(\mathbb{R}^d)$ and has bounded partial derivatives. The function $K \in L^1(\mathbb{R}^d)$ is a filter that satisfies the following conditions:

$$\text{(i) } K(x) \geq 0, \ \forall x \in \mathbb{R}^d; \qquad \text{(ii) } \int_{\mathbb{R}^d} K(x)\, dx = 1. \tag{1}$$

For any $\rho > 0$, we define K_ρ the scaled version of K by

$$K_\rho(x) := \frac{1}{\rho^d} K\left(\frac{x}{\rho}\right), \quad \forall x \in \mathbb{R}^d. \tag{2}$$

The conditions (1) still hold for any $\rho > 0$. In practice, K is usually a smoothing filter (e.g. a Gaussian) and K_ρ is a scaled version at scale ρ.

The structure tensor of u, denoted by J_ρ, is defined by

$$J_\rho := K_\rho \star \left(\nabla u \nabla u^T\right), \tag{3}$$

where ∇ denotes the gradient operator and '$\star$' is the convolution operation which acts independently on each component of the $d \times d$ tensor $\nabla u \nabla u^T$. Using the boundedness of the partial derivatives of u and the conditions (1), we have

$$|\left(J_\rho(x)\right)_{i,j}| \leq \underbrace{\left(\int_{\mathbb{R}^d} |K_\rho(x-y)|\, dy\right)}_{=1} \left(\max_{y \in \mathbb{R}^d} |(\partial_i u \partial_j u)(y)|\right) < +\infty$$

for any $x \in \mathbb{R}^d$, which implies that J_ρ is bounded in $\mathbb{R}^d$. Notice that the definition given in equation (3) differs slightly from that found in standard articles or textbooks such as [33, 34]. Therein, the image u is first convolved with a Gaussian filter and the filter K is assumed to be a Gaussian, see the discussion in Section 3.4.

A useful property of structure tensor is its positive semidefiniteness, which is a direct consequence of (1) and the convexity of the cone of symmetric positive semidefinite matrices.

Proposition 1 (Positive semidefiniteness) *The structure tensor satisfies $J_\rho(x) \succeq 0$ for any $\rho > 0$ and any $x \in \mathbb{R}^d$.*

3.2 Structure tensor and a single ellipsoid

In this section, we analyze the structure tensor behavior on a simple image whose isosurfaces are concentric ellipsoids. We show that it allows recovering its principal orientations as well as the ratios between the length of the ellipsoid main axes.

Let $\varphi : \mathbb{R}_+ \to \mathbb{R}$ denote a $\mathcal{C}^1$ function different from 0 satisfying $\varphi'(0) = 0$. Let $A \in \mathbb{R}^{d \times d}$ denote a symmetric positive-definite matrix with spectral decomposition $A = U \Sigma U^T$, where $\Sigma = \mathrm{diag}(\sigma_1^{-2}, \ldots, \sigma_d^{-2})$ and U is orthogonal. Let $x = (x_1, \ldots, x_d)$. Define $\psi : \mathbb{R}^d \to \mathbb{R}$ by

$$\psi(x) := \varphi(x^T A x), \quad \forall x \in \mathbb{R}^d. \tag{4}$$

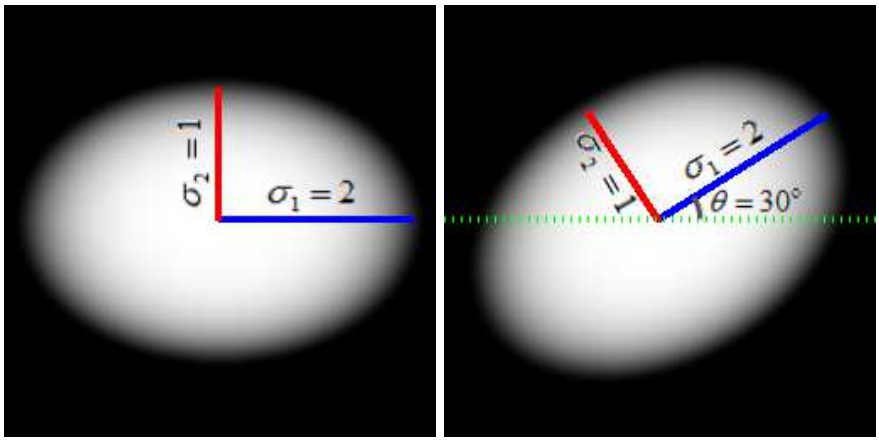

Figure 1: Representation of ψ in (4) with specific φ, U and Σ in (5)-(6). Left: the case $\sigma_1 = 2$, $\sigma_2 = 1$ and $\theta = 0°$. Right: the case $\sigma_1 = 2$, $\sigma_2 = 1$ and $\theta = 30°$.

The isosurfaces of ψ are ellipsoids in $\mathbb{R}^d$ with semiaxes of length σ_i ($i = 1, 2, \cdots, d$).

Example 1 *Let $\varphi : \mathbb{R} \to \mathbb{R}$ denote the bump function*

$$\varphi(t) = \begin{cases} \exp\left(-\frac{1}{1-t^2}\right), & \text{if } |t| < 1; \\ 0, & \text{otherwise}, \end{cases} \tag{5}$$

and let

$$U = \begin{pmatrix} \cos\theta & \sin\theta \\ -\sin\theta & \cos\theta \end{pmatrix} \quad \text{and} \quad \Sigma = \begin{pmatrix} \sigma_1^{-2} & 0 \\ 0 & \sigma_2^{-2} \end{pmatrix}. \tag{6}$$

With the above choices, the level lines of ψ in (4) are ellipses in $\mathbb{R}^2$ (see Figure 1).

Proposition 2 *Let $u := \psi$ with ψ defined in (4). Assume that $\mathrm{supp}(\psi) \subset \left[-\frac{1}{2}, \frac{1}{2}\right]^d$. Let K be the indicator of a unit disk:*

$$K(x) = \begin{cases} C_d, & \text{if } \|x\|_2 \leq 1; \\ 0, & \text{otherwise}, \end{cases} \tag{7}$$

where the normalizing constant C_d is chosen so that the normalization condition (ii) of (1) is satisfied. Then, for all $\rho \geq \sqrt{d/2}$, we have $\bar{J}_\rho(0) = \bar{A}$ and if x is small enough then $\bar{J}_\rho(x) = \bar{J}_\rho(0)$.

The above proposition leads to the following observations:

- First, for simple functions with ellipsoidal isosurfaces, a diagonalization of the structure tensor allows recovering the orientation matrix U as well as the matrix Σ up to a multiplicative constant. In 2D, it means that $\sqrt{\lambda_{\min}(J_\rho(0))/\lambda_{\max}(J_\rho(0))}$ is the ratio between the principal axes.

- Second, since this result holds for *any* function φ, the method is *contrast invariant*, which is a highly desirable property. Contrast invariance basically indicates that the method should behave similarly on different imaging devices or when using different stainings.

- Third, the structure tensor is *stable* in the sense that this result holds not only at point 0, but also in a neighborhood of 0.

3.3 Structure tensor and fields of ellipsoids

In the previous section, we focussed on a very simple image u. We now turn to a slightly more realistic setting where u is the sum of functions with ellipsoidal isosurfaces and nonoverlapping support.

We use the same notation as in the previous section and assume that $\mathrm{supp}(\psi) \subset \left[-\frac{1}{2}, \frac{1}{2}\right]^d$. The Dirac comb, denoted by Ш, is defined by

$$\text{Ш} := \sum_{x \in \mathbb{Z}^d} \delta_x,$$

where δ_x is the Dirac delta function (see e.g. [5]). Consider the image u

$$u = \text{Ш} \star \psi, \tag{8}$$

where ψ is defined in (4). The image u consists of a function ψ replicated periodically over all $\mathbb{R}^d$. Note that the translated versions of ψ do not overlap since $\mathrm{supp}(\psi) \subset \left[-\frac{1}{2}, \frac{1}{2}\right]^d$. Figure 2 illustrates such an image in the 2D case.

In Proposition 2, it is proven that $\bar{J}_\rho(0) = \bar{A}$, which implies that $J_\rho(0)$ possesses adequate information to retrieve the orientation and anisotropy of u. However, that proposition holds under the following assumptions: (i) the image u has concentric ellipsoidal isosurfaces without neighbors; (ii) the ellipsoid's center should be known. Both requirements are hardly met in practical applications. We develop below a stronger theory stating that the structure tensor allows recovering the orientation and anisotropy at *every point* of the image domain. Namely, for the image u defined in (8), we expect that $\bar{J}_\rho(x) \simeq \bar{A}$ holds at any $x \in \mathbb{R}^d$. The questions we tackle in this paragraph are the following: does the structure tensor provide an approximation of $\bar{A}$ at any point of the image domain? How many cells are necessary to reach a low approximation error?

The following proposition provides a preliminary answer.

Proposition 3 *Let K be the function defined in* (7) *and u be the image defined in* (8)*. Then $\|\bar{J}_\rho(x) - \bar{A}\|_2 = O(1/\rho)$ for all $x \in \mathbb{R}^d$.*

Proposition 3 indicates that $\bar{J}_\rho(x) \simeq \bar{A}$ for any $x \in \mathbb{R}^d$ and sufficiently large ρ. However, the asymptotic $O(1/\rho)$ convergence rate is not compelling. The following theorem shows that much more attractive results can be obtained by using smoother kernels.

Theorem 1 *Let K be the Gaussian function*

$$K(x) = \frac{1}{(2\pi)^{d/2}} \exp\left(-\frac{\|x\|_2^2}{2}\right) \tag{9}$$

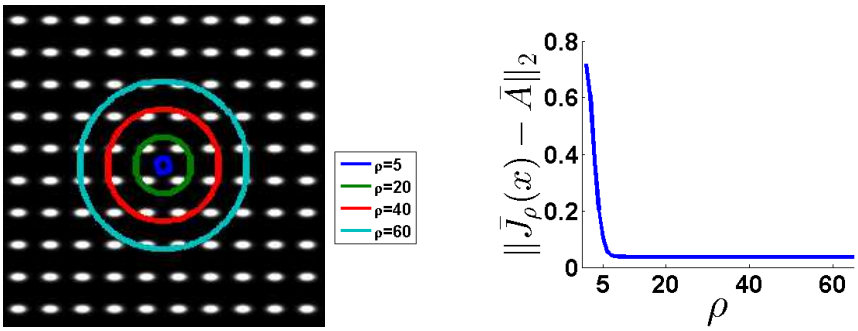

Figure 2: Left: image u defined in (8). The axes lengths of a single ellipsoid are respectively 8 and 4 pixels. Right: $\|\bar{J}_\rho(x) - \bar{A}\|_2$ w.r.t. ρ.

and u be the image defined in (8)*. Then there exits a constant $C > 0$ s.t. $\forall \rho \geq \frac{1}{2}$ and $\forall x \in \mathbb{R}^d$:*

$$\left\|\bar{J}_\rho(x) - \bar{A}\right\|_2 \leq C \exp\left(-\frac{\rho^2}{2}\right).$$

Surprisingly, the convergence of $\bar{J}_\rho(x)$ to $\bar{A}$ is extremely fast if smooth filters are exploited. Theorem 1 implies that moderate values of ρ's should produce satisfactory orientation and anisotropy estimates, and it follows from numerical experiments that a value of ρ of the order of the radius of the objects of interest is sufficient. A closer inspection at the proof of Theorem 1 reveals that the smoothness of the filter function plays a key role to control the asymptotic convergence rate.

Theorem 1 is illustrated in the 2D case in Figure 2. It shows that the magnitude $\|\bar{J}_\rho(x) - \bar{A}\|_2$ decreases to zero (up to numerical errors) extremely fast. An ellipse is around 8 pixels wide and a value of ρ around 5 provides results nearly as good as can be expected.

3.4 A note on pre-processing

As mentioned in Section 3.1, the structure tensor definition (3) is different from what is found in [33, 34]. The image u is usually pre-convolved with a Gaussian filter so as to improve the signal-to-noise-ratio. Before getting further in our investigation, let us illustrate the detrimental effect of this strategy.

Assume for simplicity that $u = \psi$ and that $\varphi(t) = \exp(-t/2)$. The image $u(x) = \exp\left(-x^T A x/2\right)$ is thus a Gaussian function with covariance matrix A^{-1}. If u is further convolved with a Gaussian filter as in [33, 34], we obtain

$$u_\sigma := K_\sigma \star u,$$

where K is the Gaussian filter defined in (9). By exploiting the facts that the convolution of Gaussian functions is still a Gaussian and that the covariance matrices sum up, we obtain

$$u_\sigma(x) \propto \exp\left(-\frac{x^T (A^{-1} + \sigma^2 \mathrm{Id})^{-1} x}{2}\right),$$

where Id is identity matrix. Consequently, pre-convolving u with a Gaussian filter shifts the eigenvalues of A by a quantity σ^2. This, in turn, results in biased

anisotropy estimates. For instance, in the 2D case, the structure tensor based anisotropy obtained using u_σ is

$$\left(\frac{\lambda_{\max}^{-1}(A)+\sigma^2}{\lambda_{\min}^{-1}(A)+\sigma^2}\right)^{1/2},$$

which is different from the ground truth anisotropy $\left(\frac{\lambda_{\min}(A)}{\lambda_{\max}(A)}\right)^{1/2}$.

The simple analysis above shows that in practice, more advanced image denoising techniques that keep isosurfaces unchanged should be preferred over a simple convolution with a Gaussian filter. A wide choice is now available such as anisotropic diffusion, total variation denoising, frame based regularization or non-local methods [31, 27, 29, 7, 8].

4 Numerical validation

In this section, we conduct some numerical experiments to evaluate the structure tensors performance on synthetic and real data. The main biological problem addressed in our experiments is the analysis of geometrical configurations of nuclei in multicellular tumor spheroids. There are at least two reasons making this analysis relevant. First, tumor development is associated with a disorganization of the tissue. The role played by this disorganization is not well understood yet and it has been shown that it could have an impact on tumor cell behavior [36]. Second, among the key parameters involved in tumor growth, those related to mechanical forces seem to play a critical role [21, 30, 9]. The elongation of nuclei in a preferential direction is an indicator of local stresses [14, 32]. Assessing the anisotropy and orientation of nuclei in their micro-environment is therefore crucial to better understand tumor organization and mechanics.

4.1 Implementation details

Up to now, we only performed theoretical analyses in the continuous domain. In practice, the structure tensor should be adapted to the discrete setting.

The discrete gradient operator ∇ is defined by $\nabla = \begin{pmatrix}\partial_1\\ \vdots \\ \partial_d\end{pmatrix}$. In all reported experiments, the partial differential operators ∂_i are defined as convolutions with discrete kernels. From an asymptotic point of view any kernel leading to a consistent discretization should provide good results. However, the kernel design turns out to be crucial to provide good orientation and anisotropy estimates. Key properties of discrete kernels are [35]: i) *rotation invariance*, ensuring a reliable orientation estimation, ii) *separability*, ensuring faster computations and iii) *no shift*, implying the use of centered finite differences. Following these criteria, the authors of [35] suggested to use the following filter in 2D:

$$h = \frac{1}{32}\begin{pmatrix}-3 & 0 & 3\\ -10 & 0 & 10\\ -3 & 0 & 3\end{pmatrix}.$$

i.e. to set $\partial_1 u = h \star u$ and $\partial_2 u = h^T \star u$. Using the same methodology in 3D, one can derive the following filter (using Matlab notation):

$$h(:,:,1) = \begin{pmatrix} 0.0153 & 0 & -0.0153 \\ 0.0568 & 0 & -0.0568 \\ 0.0153 & 0 & -0.0153 \end{pmatrix},$$
$$h(:,:,2) = \begin{pmatrix} 0.0568 & 0 & -0.0568 \\ 0.2117 & 0 & -0.2117 \\ 0.0568 & 0 & -0.0568 \end{pmatrix}$$

and $h(:,:,3) = h(:,:,1)$.

The gradient is computed in the space domain, while the convolution with K_ρ is based on fast Fourier transforms. The overall computational complexity for an image with n pixels is therefore $\mathcal{O}(n \log(n))$. In practice, the structure tensor can be computed in near real-time for 2D images and takes a few seconds for 3D images. It can be very easily parallelized on multicore or GPU architectures. All codes were written in MATLAB 7.9 and experiments were conducted on a Lenovo personal computer with Intel Core (TM) CPU 2.30GHZ and 8G memory.

4.2 2D and 3D synthetic data

In order to validate the theory, we first concentrate on 2D and 3D synthetic tumor spheroids.

4.2.1 Synthesizing images

A tumor spheroid image $u : \mathbb{R}^d \to \mathbb{R}_+$ is synthesized by

$$u(x) = \sum_{i=1}^{N} \varphi\left((x - x_i^c)^T A_i (x - x_i^c)\right), \quad \forall x \in \mathbb{R}^d, \tag{10}$$

where N is the number of nuclei in the spheroid; φ is the bump function defined in (5); and $x_i^c \in \mathbb{R}^d$ is the i-th nucleus center. The centers are drawn at random in a d-dimensional sphere in such a way that the nuclei do not overlap.

- If $d = 2$, the matrix $A_i \succ 0$ is defined by

$$A_i = R^{\theta_i} \mathrm{diag}(\sigma_{1,i}^{-2}, \sigma_{2,i}^{-2})(R^{\theta_i})^T. \tag{11}$$

  where R^{θ_i} is the Givens transform (see Section 2); θ_i is the phase angle of the radial line issued from the origin and crossing the nucleus center x_i^c, see Fig. 1.

- If $d = 3$, the matrix $A_i \succ 0$ is defined by

$$A_i = R_{1,2}^{\theta_i} R_{2,3}^{\gamma_i} \mathrm{diag}(\sigma_{1,i}^{-2}, \sigma_{2,i}^{-2}, \sigma_{3,i}^{-2})(R_{1,2}^{\theta_i} R_{2,3}^{\gamma_i})^T, \tag{12}$$

  where θ_i, γ_i denote the compass and elevation angles of the radial line crossing the ellipsoid center.

The anisotropy of the i-th nucleus is defined by

$$\alpha_i := \frac{\min\limits_{k=1,2,\cdots,d} \sigma_{k,i}}{\max\limits_{k=1,2,\cdots,d} \sigma_{k,i}}. \tag{13}$$

In our 2D experiment, the anisotropy α_i increases linearly from the image center to the outer layers of the sphere. For the 3D case, the anisotropy α_i is set as constant. Figure 3(a) and Figure 6 (a)-(b) display the 2D and 3D synthetic spheroids respectively.

4.2.2 Measuring the performance

In order to assess the structure tensor efficiency, we evaluate the following quantities:

- **Orientation.** Let $\tilde{v}_i$ denote the eigenvector corresponding to the largest eigenvalue of $J_\rho(x_i^c)$ and $v_i = (\cos\theta_i, \sin\theta_i)$ denote the ground truth orientation. The following angles

  $$\angle(\tilde{v}_i, v_i), \quad i = 1, 2, \cdots, N, \tag{14}$$

  are used to evaluate the orientation accuracy in 2D. An angle close to $0°$ indicates a good orientation estimation, while an angle close to $90°$ is the worst possible estimate. For the 3D case, we choose for $\tilde{v}_i$ either the largest eigenvector (prolate spheroid) ot the smallest eigenvector (oblate spheroid).

- **Anisotropy**. The structure tensor based anisotropy is defined by $\tilde{\alpha}_i = \left(\frac{\lambda_{\min}(J_\rho(x_i^c))}{\lambda_{\max}(J_\rho(x_i^c))}\right)^{1/2}$. The ratio

  $$\tilde{\alpha}_i/\alpha_i, \quad i = 1, 2, \cdots, N, \tag{15}$$

  is used to quantify the estimated anisotropy accuracy, where α_i is ground-truth anisotropy, see (13). A ratio close to 1 indicates that the anisotropy is correctly evaluated.

- **Spectral norm**. In the experiments based on synthetic images, a matrix $A(x)$ can be associated to every point of the image domain. We can therefore evaluate the spectral norm $\|\bar{J}_\rho(x) - \bar{A}(x)\|_2$ everywhere and not only at the nuclei centers.

4.2.3 2D synthetic data

We report numerical results on the 2D synthetic spheroid displayed in Figure 3(a). The spheroid is first approximated by the nuclei convex hull, denoted by $\mathcal{H}$. The green curve in Figure 3(d) represents the convex hull boundary[1], denoted by $\partial\mathcal{H}$. Note that the upcoming analyses are all restricted to the convex hull.

[1] In MATLAB, this result can be obtained by first thresholding the image and then using the quickhull algorithm [2] (*convhull* command).

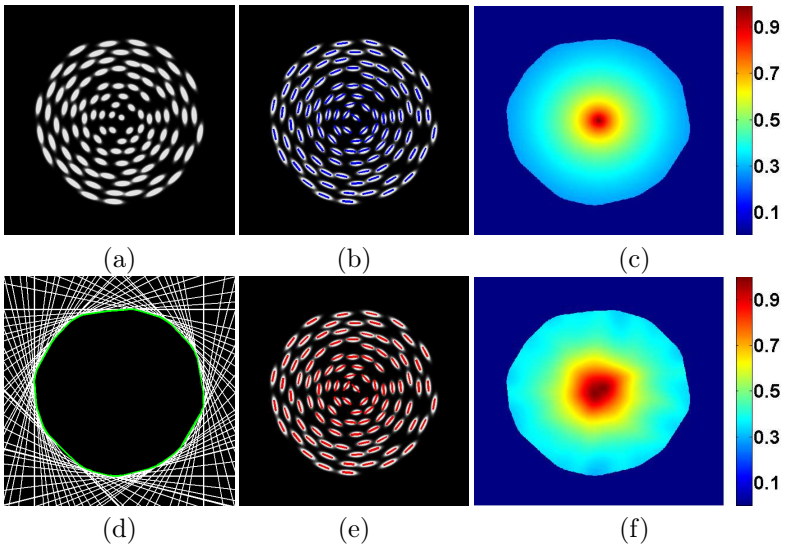

Figure 3: 2D synthetic data (a) 512×512 synthetic tumor spheroid (b) ground-truth orientations (c) ground-truth anisotropy (d) ground-truth orientations (e) Structure tensor based orientations (f) Structure tensor based anisotropy.

We use the value $\rho = 5$ in (3), this value is to be compared with the small axis of the ellipses that is $\sigma_1 = 10$ and the large axis which ranges σ_2 from 10 to 32. An adequate value for ρ is of the order of the radius of the objects of interest. Figure 3 (e)-(f) show the structure tensor based orientations and anisotropies which should be compared to the ground truth ones in Figure 3 (b)-(c). The orientations and anisotropy are clearly very well estimated. This is somehow surprising since for this image, only a small number of cells share the same orientation and anisotropy locally. This favorable behavior is another illustration of the fast convergence speed obtained in Theorem 1.

To further quantify the accuracy of the results, the quantities (14)-(15) are evaluated. The histograms of both quantities are displayed in Figure 4. They show that approximately 95% of estimated orientations have an angular error below 4°. Similarly, approximately 65% of estimated anisotropies have a an error below 10%.

Finally, when using synthetic data, a ground-truth structure tensor $A(x)$ can be defined at every point of the image domain. We can thus compare the four coefficients of the 2×2 matrix $\bar{A}(x)$ with the coefficients of $\bar{J}_\rho$. The distance $\|\bar{J}_\rho - \bar{A}\|_2$ can also be evaluated at every point of the image domain, see Figure 5. We observe that the structure tensor approximates accurately the ground truth tensor.

4.2.4 3D synthetic data

We now test the structure tensor efficiency on 3D synthetic data generated by formula (12), see Figures 6(a) for an oblate example and (b) for a prolate example. The structure tensor J_ρ is computed with $\rho = 5$. The estimated orientations are displayed in Figure 6 (e) and (f) while the ground truth orien-

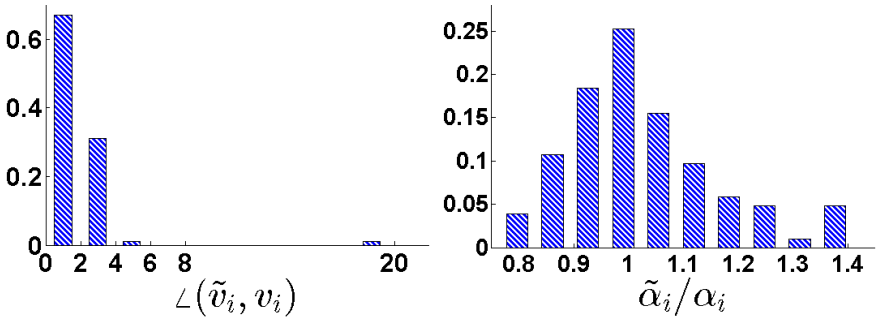

Figure 4: Analysis of structure tensor based accuracy for the 2D test case. Histograms of orientations errors (left) and of anisotropy errors (right).

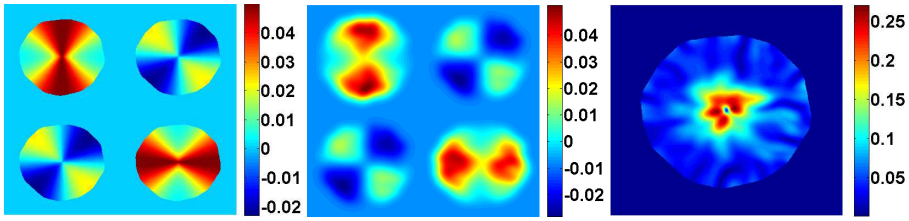

Figure 5: Four coefficients of matrix $\bar{A}$ (left), four coefficients of matrix $\bar{J}_\rho$ (center) and error map $\|\bar{J}_\rho - \bar{A}\|_2$ (right).

tations are displayed in Figure 6 (c) and (d). The orientation is well retrieved. This is also confirmed by the histogram in Figure 7. Moreover, the histogram of anisotropy discrepancies show that approximately 70% of the anisotropies are evaluated with an error below 10%. Overall, these results confirm that the structure tensor is also very attractive to estimate anisotropies and orientations for 3D data.

4.3 Performance evaluation on real spheroid images

We now evaluate the structure tensor based orientation and anisotropy on a 2D real image. The image that we use in our experiment contains 1465 nuclei. The 'gold standard' reference was obtained manually. The scalar ρ is set to 10 in this section. This value was selected manually and corresponds roughly to the radius of the nuclei.

The gold standard and estimated orientations are displayed in Figure 8. The orientation and anisotropy errors are presented in Figure 9(a) and (b) respectively.

Let us emphasize that the gold standard is subject to many errors since i) a preferential orientation cannot be defined properly on isotropic cells and ii) fitting a thousand ellipses manually is subject to many errors. Moreover, real data strongly depart from the ideal models considered in Section 3 since (i) the SNR of real tumor spheroid image is typically low due to noise, blur, variations in illumination, etc; (ii) the nuclei geometry is only approximately ellipsoidal; (iii) the nuclei may overlap in 2D. Despite the rather poor quality of

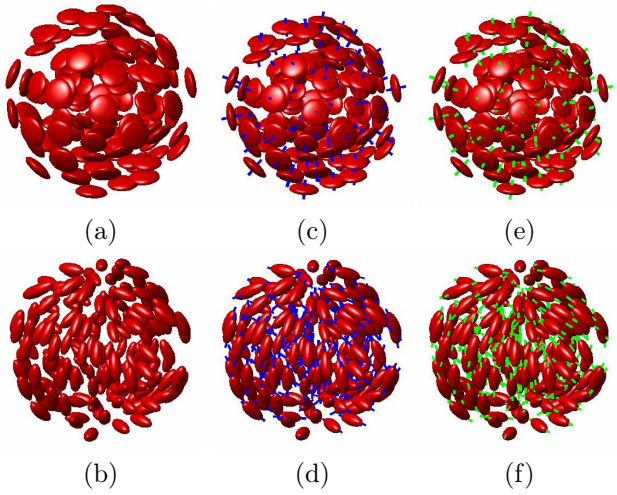

Figure 6: 3D synthetic data (size: $128 \times 128 \times 128$). (a) spheroid with $\sigma_1 : \sigma_2 : \sigma_3 = 5 : 5 : 2$. (b) spheroid with $\sigma_1 : \sigma_2 : \sigma_3 = 5 : 2 : 2$. (c)-(d) ground truth orientations of spheroids (a) and (b) respectively. (e)-(f) structure tensor based orientations.

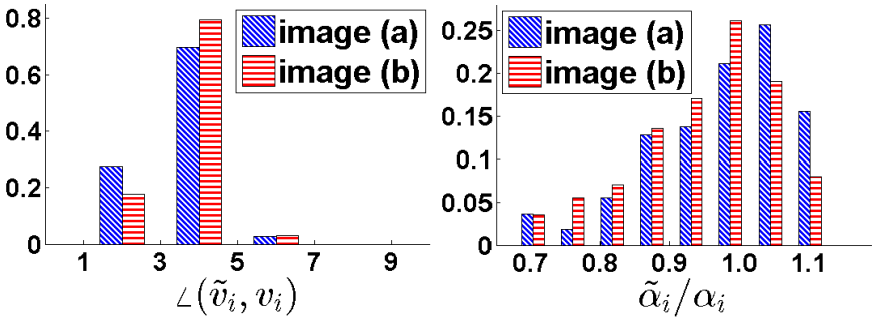

Figure 7: Analysis of structure tensor based errors for 3D synthetic data from Figure 6. Histograms of orientations errors (left) and of anisotropy errors (right).

data and gold standard, the results fit remarkably well. Overall the orientation is evaluated with an error no larger 20° while the anisotropy seldom exceeds 50% error. Finally, note that the preferential orientation is not well defined at the image center since cells are near isotropic.

In Figure 9(c) we plot the median, mean and 25% $\sim$ 75% percentiles of the angle error (14) with respect to the distance to the spheroid boundary. The notation 'dist$(x_i^c, \partial\mathcal{H})$' stands for the Euclidean distance from the nucleus center x_i^c to the spheroid boundary. Figure 9(c) indicates that structure tensor provides accurate orientations near the spheroid boundary and less accurate in the center, since the median error increases from 7° close to the boundary to 14° near the center.

4.4 Application to drug effects analysis on spheroids

As a proof of concept, spheroids were treated with latrunculin A, an inhibitor of actin polymerization. The comparison of (a) and (e) in Figure 10 shows that this treatment induces a disorganization. We applied the structure tensor to extract the orientation and anisotropy maps in Figure 10 (c), (d), (g) and (h). The angle is measured with respect to the normal of the closest point of the boundary. In other words, an angle equal to 90° means that the local orientation is parallel to the boundary, and an angle equal to 0° means that the local orientation is normal to the boundary.

The results obtained show a decrease of both nuclei anisotropy and alignment with the spheroid boundary in the outer layers after treatment. This observation is confirmed by the graphs showed in Figure 11. In Figure 11(a) we compare the alignement of the nuclei with respect to the boundary with or without treatment. In Figures 11(b) and (c) we present the alignment with respect to the distance to the boundary. We observe that the mean angle at the origin is around 80° for the control spheroid and 60° for the treated spheroid, indicating that the drug tends to desalign the nuclei with respect to the spheroid boundary. Moreover, in Figure 11 (b), the gray zone is narrow at the origin, reflecting the fact that nearly all nuclei near are well aligned with the boundary in the outer layers. On the contrary, the gray zone at the origin of the graph in Figure 11 (c) is thick, indicating that the orientation is much more erratic.

In Figure 11(d) we present the distribution of anisotropy for the control and the treated spheroid. In Figures 11 (e) and (f) we present the anisotropy with respect to the distance to the boundary. We observe that the mean anisotropy near the spheroid boundary is approximately equal to 0.6 for the control spheroid and 0.8 for the treated spheroid, indicating that nuclei are more round for the treated case.

As a summary, our methodology allows quantifying both the change of alignment and the decrease of anisotropy and could therefore have interesting applications in high content throughput.

5 Outlook

We proposed an original theoretical analysis of structure tensors, justifying their use for evaluating orientations and anisotropies of cells or nuclei in 2D or 3D images. Our theoretical results were validated by numerical experiments, on

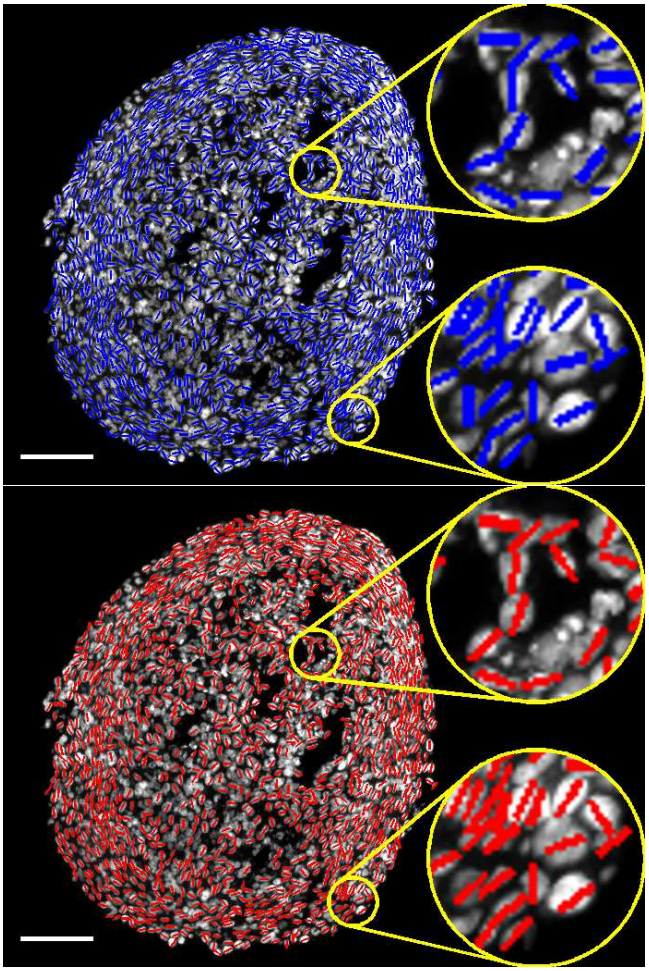

Figure 8: Comparison of ground truth orientations (top) and estimated orientations (bottom) on spheroid sections. Nuclei are stained using DAPI. Images were acquired using epifluorescence microscope (LEICA DM5000) and 10X objective NA:0.3. Scale bar: 100μm.

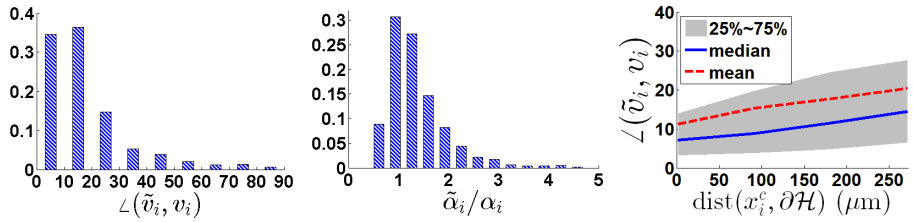

Figure 9: Quantification of structure tensor based results for the 2D experimental test case. (a) histogram of orientation error, (b) histogram of anisotropy error, (c) structure tensor based orientations with respect to nuclei locations.

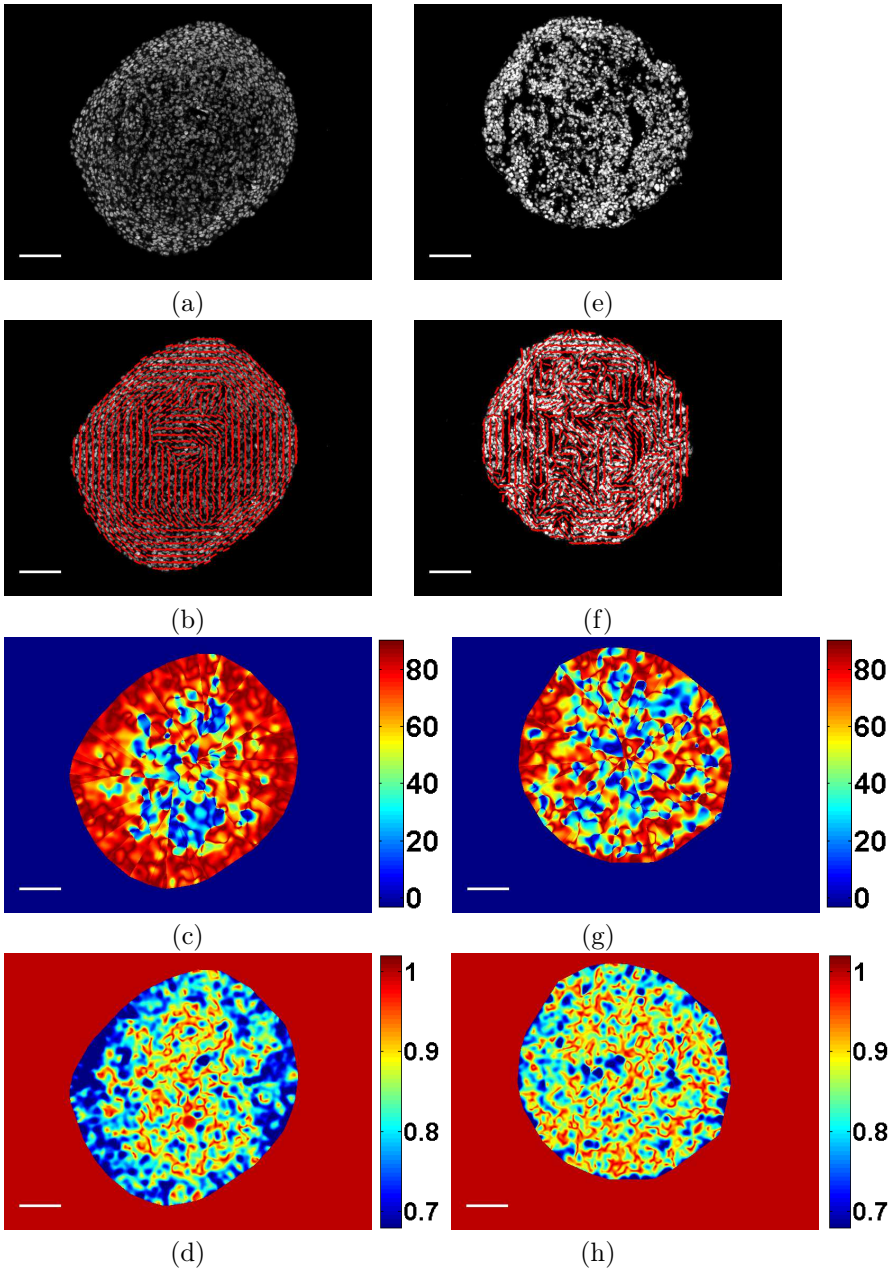

Figure 10: (a) and (e): Images of Tumor spheroids cryosections with nuclei labelled using DAPI. Images were obtained as in Figure 8. Top row: control spheroid (with no drug). Bottom row: treated with latrunculin. (b) and (f): orientation map. (c) and (g): angle maps. An angle equal to 90° indicates that nuclei are aligned with the spheroid boundary. (d) and (h) anisotropy map. Scale bar: 100μm.

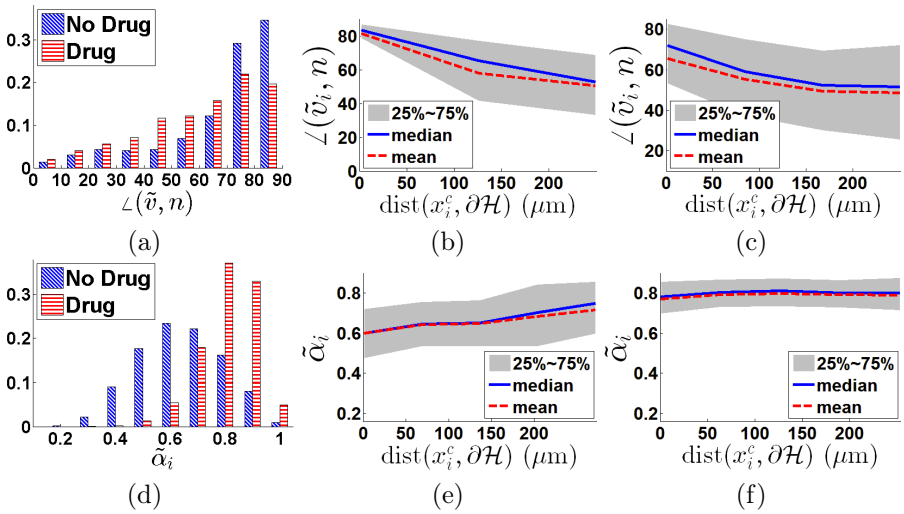

Figure 11: Structure tensor based orientations for the control and treated spheroids. (a) histogram of the orientation with respect to the normal at the closest point on the boundary. (b) and (c) distribution of orientations w.r.t. the distance to the boundary for the no-drug and drug cases respectively. (d) histograms of anisotropy. (e) and (f) distributions of anisotropies w.r.t. the distance to the boundary for the no-drug and drug cases respectively.

synthetic and real data. Overall the present work shows that the structure tensor provides a fast, simple, robust and user friendly method for biomedical imaging. To finish, let us add a few remarks:

- First, cells or nuclei are not the only ellipsoid like objects and the method can actually be applied in any field where such objects appear (e.g. lobules in adipose tissues).
- Second, our results show that the structure tensor can be used as a pre-processing tool for segmentation methods. Knowing the rough orientation, anisotropy and volume of a cell can provide an initialization for more advanced segmentation techniques. For instance, it is fundamental to have a first rough segmentation in random based optimization methods [28] .
- Finally, more and more mathematical models describe tissues as continuous media. The information contained in the structure tensor is itself continuous and therefore seems easy to use in data assimilation problems. This opens interesting perspectives to understand tissue biomechanics for instance. We plan to further investigate this problem in forthcoming works.

A Proof of Proposition 2

Simple calculation lead to

$$\nabla\psi(x) = 2\varphi'(x^T Ax)Ax.$$

Therefore

$$\begin{aligned} J_\rho(0) &= \int_{\mathbb{R}^d} K_\rho(-x)(\nabla\psi\nabla\psi^T)(x)\,dx \\ &= 4A\left(\int_{\mathbb{R}^d} (\varphi'(x^TAx))^2 xx^T K_\rho(x)\,dx\right)A^T. \end{aligned}$$

But if $\rho > \sqrt{d/2}$ then K_ρ is constant on the domain where ψ does not vanish. Therefore by using the change of variable $y = \Sigma^{\frac{1}{2}}U^Tx$, we obtain:

$$\begin{aligned} J_\rho(0) &\propto |\Sigma^{-\frac{1}{2}}|AU\Sigma^{-\frac{1}{2}} \underbrace{\left(\int_{\mathbb{R}^d} \varphi'(\|y\|_2^2)^2 yy^T\,dy\right)}_{\propto \mathrm{Id}} \Sigma^{-\frac{1}{2}}U^TA^T \\ &\propto A. \end{aligned}$$

Since K_ρ is constant on a neighborhood of the domain where ψ does not vanish, J_ρ is invariant by small translations hence J_ρ is locally constant around 0.

B Proof of Proposition 3

We denote $B(x_0,\rho) = \{x \mid \|x - x_0\|_2 \leq \rho\}$ the Euclidian ball centered at x_0 with radius ρ and $S(x_0,\rho) = \{x \mid \|x - x_0\|_2 \leq \rho\}$ the Euclidian sphere centered at x_0 with radius ρ. We have

$$J_\rho(x_0) = \frac{1}{\rho^d}\int_{B(x_0,\rho)} (\nabla u\nabla u^T)(x)\,dx.$$

The image u is a sum of (non-overlapping) replicates of ψ. From Proposition 2, we know that all the replicates of ψ with support included in $B(x_0,\rho)$ will have a contribution to $J_\rho(x)$ proportional to A while the ones with support intersecting $S(x_0,\rho)$ have a contribution that can be considered as a bias, whose components are bounded by $\int_{\mathbb{R}^d} |\partial_i\psi\partial_j\psi|(x)\,dx$. Let $\mathcal{I} = \{i \in \mathbb{Z}^d \mid \mathrm{supp}(\psi(\cdot - i)) \subset B(x_0,\rho)\}$ and $\mathcal{J} = \{j \in \mathbb{Z}^d \mid \mathrm{supp}(\psi(\cdot - j)) \cap S(x_0,\rho) \neq \emptyset\}$. For sufficiently large ρ, $|\mathcal{I}| \propto \rho^d$ (the volume of a ball of radius ρ) while $|\mathcal{J}| \propto \rho^{d-1}$ (the area of the sphere). Therefore

$$J_\rho(x_0) \propto (\rho^d A + \rho^{d-1}B_\rho)/\rho^d,$$

where B_ρ is some bias of bounded amplitude. This implies that

$$\|\bar{J}_\rho(x_0) - \bar{A}\|_2 = \mathcal{O}\left(1/\rho\right).$$

C Proof of Theorem 1

The non-smoothed structure tensor is defined by

$$\begin{aligned} J_0 &= \nabla u\nabla u^T \\ &= (\text{Ш} \star \nabla\psi)\cdot(\text{Ш} \star \nabla\psi)^T \\ &= \left((\partial_i\psi\partial_j\psi) \star \text{Ш}\right)_{i,j}, \end{aligned}$$

where the last equality follows from the fact that the functions are nonoverlapping. By exploiting the facts that $J_\rho = K_\rho \star J_0$ and $\widehat{\text{Ш}} = \text{Ш}$, it comes that

$$\begin{aligned}\hat{J}_\rho &= \left((\widehat{\partial_i\psi\partial_j\psi}) \cdot \widehat{\text{Ш}} \cdot \widehat{K_\rho}\right)_{1\leq i,j\leq d} \\ &= \left(\sum_{k\in\mathbb{Z}^d} (\widehat{\partial_i\psi\partial_j\psi})(k)\widehat{K_\rho}(k)\delta_k\right)_{1\leq i,j\leq d}.\end{aligned}$$

This analysis provides a Fourier series decomposition of J_ρ:

$$J_\rho(x) = \left(\sum_{k\in\mathbb{Z}^d} (\widehat{\partial_i\psi\partial_j\psi})(k)\widehat{K_\rho}(k)\exp(-2i\pi\langle x,k\rangle)\right)_{1\leq i,j\leq d}.$$

Moreover (1)-(ii) implies that $\widehat{K_\rho}(0) = 1$, and for all i, j:

$$\begin{aligned}&\left|(J_\rho(x))_{i,j} - (\widehat{\partial_i\psi\partial_j\psi})(0)\right| \\ &= \left|\sum_{k\in\mathbb{Z}^d\setminus\{0\}} (\widehat{\partial_i\psi\partial_j\psi})(k)\widehat{K_\rho}(k)\exp(-2i\pi\langle x,k\rangle)\right| \\ &\leq \sum_{k\in\mathbb{Z}^d\setminus\{0\}} \left|(\widehat{\partial_i\psi\partial_j\psi})(k)\right|\left|\widehat{K_\rho}(k)\right|\end{aligned}$$

By denoting $y = \Sigma^{\frac{1}{2}}U^T x$, we obtain:

$$\begin{aligned}&\left(\widehat{\partial_i\psi\partial_j\psi})(0)\right)_{1\leq i,j\leq d} \\ &= \left(\int_{\mathbb{R}^d} (\partial_i\psi\partial_j\psi)(x)\right)_{1\leq i,j\leq d} \\ &= 4A\left(\int_{\mathbb{R}^d} \varphi'(x^TAx)^2 xx^T\,dx\right)_{1\leq i,j\leq d} A^T \\ &= 4|\Sigma^{-\frac{1}{2}}|AU\Sigma^{-\frac{1}{2}} \underbrace{\left(\int_{\mathbb{R}^d} \varphi'(\|y\|_2^2)yy^T\,dx\right)_{1\leq i,j\leq d}}_{\propto \mathrm{Id}} \Sigma^{-\frac{1}{2}}U^TA^T \\ &\propto A.\end{aligned}$$

Since $\psi \in \mathcal{C}^1$ with bounded support, $c = \|\partial_i\psi\partial_j\psi\|_1 < +\infty$. Therefore $\|\widehat{\partial_i\psi\partial_j\psi}\|_\infty \leq c$. Moreover, $\widehat{K_\rho}(k) = \widehat{K}(\rho k)$ so that

$$\begin{aligned}\sum_{k\in\mathbb{Z}^d\setminus\{0\}} \left|(\widehat{\partial_i\psi\partial_j\psi})(k)\right|\left|\widehat{K_\rho}(k)\right| &\leq c\sum_{k\in\mathbb{Z}^d\setminus\{0\}} |\widehat{K_\rho}(k)| \\ &= c\sum_{k\in\mathbb{Z}^d\setminus\{0\}} |\widehat{K}(\rho k)| \\ &\propto \sum_{k\in\mathbb{Z}^d\setminus\{0\}} \exp\left(-\frac{\rho^2\|k\|_2^2}{2}\right).\end{aligned}$$

We now remark that

$$\begin{aligned}\sum_{k\in\mathbb{Z}^d}\exp\left(-\frac{\rho^2\|k\|_2^2}{2}\right) &= \left(\sum_{j\in\mathbb{Z}}\exp\left(-\frac{\rho^2 j^2}{2}\right)\right)^d\\ &= \left(1+2\sum_{j\geq 1}\exp\left(-\frac{\rho^2 j^2}{2}\right)\right)^d\\ &= (1+2u(\rho))^d\\ &= 1+2du(\rho)+O_{\rho\to+\infty}(u(\rho))\end{aligned}$$

where

$$u(\rho)=\sum_{j\geq 1}\exp\left(-\frac{\rho^2 j^2}{2}\right)\leq\sum_{j\geq 1}\exp\left(-\frac{\rho^2 j}{2}\right)=\frac{\exp(-\frac{\rho^2}{2})}{1-\exp(-\frac{\rho^2}{2})}.$$

Since $u(\rho)$ is asymptotic to $\exp(-\frac{\rho^2}{2})$ when $\rho\to\infty$ the claim is proved.

Acknowledgement

The authors would like to thank the TRI-Genotoul and ITAV-USR3505 image facilities and all the members of ITAV for providing a nice research environment.

Funding This work was supported by the ANR SPH-IM-3D (ANR-12-BSV5-0008), the NNSFC Grant 11301055 and la Fondation pour la Recherche Médicale (équipe labelisée 2012). A. D. is recipient of a doctoral fellowship from the Association pour la Recherche contre le Cancer and is as student of the école de l'INSERM Liliane Bettencourt.

References

[1] D Ambrosi and F Mollica. On the mechanics of a growing tumor. *International Journal of Engineering Science*, 40(12):1297–1316, 2002.

[2] C Bradford Barber, David P Dobkin, and Hannu Huhdanpaa. The quickhull algorithm for convex hulls. *ACM Transactions on Mathematical Software (TOMS)*, 22(4):469–483, 1996.

[3] Josef Bigun, Goesta H Granlund, and Johan Wiklund. Multidimensional orientation estimation with applications to texture analysis and optical flow. *Pattern Analysis and Machine Intelligence, IEEE Transactions on*, 13(8):775–790, 1991.

[4] Isabelle Bonnet, Philippe Marcq, Floris Bosveld, Luc Fetler, Yohanns Bellaïche, and François Graner. Mechanical state, material properties and continuous description of an epithelial tissue. *Journal of The Royal Society Interface*, page rsif20120263, 2012.

[5] Ronald N Bracewell. The fourier transform and its applications. McGraw-Hill, 1978.

[6] Didier Bresch, Thierry Colin, Emmanuel Grenier, Benjamin Ribba, Olivier Saut, et al. A viscoelastic model for avascular tumor growth. 2009.

[7] Antoni Buades, Bartomeu Coll, and J-M Morel. A non-local algorithm for image denoising. In *Computer Vision and Pattern Recognition, 2005. CVPR 2005. IEEE Computer Society Conference on*, volume 2, pages 60–65. IEEE, 2005.

[8] Kostadin Dabov, Alessandro Foi, Vladimir Katkovnik, and Karen Egiazarian. Image denoising by sparse 3-d transform-domain collaborative filtering. *Image Processing, IEEE Transactions on*, 16(8):2080–2095, 2007.

[9] Annaïck Desmaison, Céline Frongia, Katia Grenier, Bernard Ducommun, and Valérie Lobjois. Mechanical stress impairs mitosis progression in multi-cellular tumor spheroids. *PloS one*, 8(12):e80447, 2013.

[10] Salvatore Federico and T Christian Gasser. Nonlinear elasticity of biological tissues with statistical fibre orientation. *Journal of the Royal Society Interface*, 7(47):955–966, 2010.

[11] Edouard Fonck, Georg G Feigl, Jean Fasel, Daniel Sage, Michael Unser, Daniel A Rüfenacht, and Nikolaos Stergiopulos. Effect of aging on elastin functionality in human cerebral arteries. *Stroke*, 40(7):2552–2556, 2009.

[12] Wolfgang Förstner and Eberhard Gülch. A fast operator for detection and precise location of distinct points, corners and centres of circular features. In *Proc. ISPRS intercommission conference on fast processing of photogrammetric data*, pages 281–305, 1987.

[13] Gösta H Granlund and Hans Knutsson. *Signal processing for computer vision*, volume 2. Springer, 1995.

[14] Farshid Guilak. Compression-induced changes in the shape and volume of the chondrocyte nucleus. *Journal of biomechanics*, 28(12):1529–1541, 1995.

[15] Chris Harris and Mike Stephens. A combined corner and edge detector. In *Alvey vision conference*, volume 15, page 50. Manchester, UK, 1988.

[16] JD Humphrey. Review paper: Continuum biomechanics of soft biological tissues. *Proceedings of the Royal Society of London. Series A: Mathematical, Physical and Engineering Sciences*, 459(2029):3–46, 2003.

[17] JD Humphrey and KR Rajagopal. A constrained mixture model for growth and remodeling of soft tissues. *Mathematical models and methods in applied sciences*, 12(03):407–430, 2002.

[18] Raphael Jorand, Gwénaële Le Corre, Jordi Andilla, Amina Maandhui, Céline Frongia, Valérie Lobjois, Bernard Ducommun, and Corinne Lorenzo. Deep and clear optical imaging of thick inhomogeneous samples. *PloS one*, 7(4):e35795, 2012.

[19] Bruce D Lucas and Takeo Kanade. An iterative image registration technique with an application to stereo vision. In *IJCAI*, volume 81, pages 674–679, 1981.

[20] Andreas Menzel, Magnus Harrysson, and Matti Ristinmaa. Towards an orientation-distribution-based multi-scale approach for remodelling biological tissues. *Computer methods in biomechanics and biomedical engineering*, 11(5):505–524, 2008.

[21] Fabien Montel, Morgan Delarue, Jens Elgeti, Laurent Malaquin, Markus Basan, Thomas Risler, Bernard Cabane, Danijela Vignjevic, Jacques Prost, Giovanni Cappello, et al. Stress clamp experiments on multicellular tumor spheroids. *Physical review letters*, 107(18):188102, 2011.

[22] Nicolas Olivier, Miguel A Luengo-Oroz, Louise Duloquin, Emmanuel Faure, Thierry Savy, Israël Veilleux, Xavier Solinas, Delphine Débarre, Paul Bourgine, Andrés Santos, et al. Cell lineage reconstruction of early zebrafish embryos using label-free nonlinear microscopy. *Science*, 329(5994):967–971, 2010.

[23] Kannappan Palaniappan, Ilker Ersoy, and Sumit K Nath. Moving object segmentation using the flux tensor for biological video microscopy. In *Advances in Multimedia Information Processing–PCM 2007*, pages 483–493. Springer, 2007.

[24] Sorin Pop, Alexandre C Dufour, Jean-François Le Garrec, Chiara V Ragni, Clémire Cimper, Sigolène M Meilhac, and Jean-Christophe Olivo-Marin. Extracting 3d cell parameters from dense tissue environments: application to the development of the mouse heart. *Bioinformatics*, 29(6):772–779, 2013.

[25] A Ravishankar Rao and Brian G. Schinck. Computing oriented texture fields. *CVGIP: Graphical Models and Image Processing*, 53(2):157–185, 1991.

[26] Rana Rezakhaniha, Aristotelis Agianniotis, Jelle Tymen Christiaan Schrauwen, Alessandra Griffa, Daniel Sage, CVC Bouten, FN Van de Vosse, Michaël Unser, and Nikolaos Stergiopulos. Experimental investigation of collagen waviness and orientation in the arterial adventitia using confocal laser scanning microscopy. *Biomechanics and modeling in mechanobiology*, 11(3-4):461–473, 2012.

[27] Leonid I Rudin, Stanley Osher, and Emad Fatemi. Nonlinear total variation based noise removal algorithms. *Physica D: Nonlinear Phenomena*, 60(1):259–268, 1992.

[28] Emmanuel Soubies, Pierre Weiss, and Xavier Descombes. A 3d segmentation algorithm for ellipsoidal shapes. application to nuclei extraction. In *Proceedings ICPRAM*, 2013.

[29] J-L Starck, Emmanuel J Candès, and David L Donoho. The curvelet transform for image denoising. *Image Processing, IEEE Transactions on*, 11(6):670–684, 2002.

[30] Triantafyllos Stylianopoulos, John D Martin, Vikash P Chauhan, Saloni R Jain, Benjamin Diop-Frimpong, Nabeel Bardeesy, Barbara L Smith, Cristina R Ferrone, Francis J Hornicek, Yves Boucher, et al. Causes, consequences, and remedies for growth-induced solid stress in murine and human tumors. *Proceedings of the National Academy of Sciences*, 109(38):15101–15108, 2012.

[31] David Tschumperlé. Fast anisotropic smoothing of multi-valued images using curvature-preserving pde's. *International Journal of Computer Vision*, 68(1):65–82, 2006.

[32] Marie Versaevel, Thomas Grevesse, and Sylvain Gabriele. Spatial coordination between cell and nuclear shape within micropatterned endothelial cells. *Nature communications*, 3:671, 2012.

[33] Joachim Weickert. *Anisotropic diffusion in image processing*, volume 1. Teubner Stuttgart, 1998.

[34] Joachim Weickert. Coherence-enhancing diffusion filtering. *International Journal of Computer Vision*, 31(2-3):111–127, 1999.

[35] Joachim Weickert and Hanno Scharr. A scheme for coherence-enhancing diffusion filtering with optimized rotation invariance. *Journal of Visual Communication and Image Representation*, 13(1):103–118, 2002.

[36] Britta Weigelt and Mina J Bissell. Unraveling the microenvironmental influences on the normal mammary gland and breast cancer. In *Seminars in cancer biology*, volume 18, pages 311–321. Elsevier, 2008.